J Nanopart Res (2013) 15:1343
DOI 10.1007/s11051-012-1343-1

RESEARCH PAPER

Experimental evidences of substitutional solution of Er dopant in Er-doped SnO_2 nanoparticles

F. H. Aragón · J. A. H. Coaquira · P. Hidalgo · R. Cohen · L. C. C. M. Nagamine · S. W. da Silva · P. C. Morais · H. F. Brito

Received: 21 August 2012 / Accepted: 23 November 2012 / Published online: 11 December 2012

Abstract Structural and hyperfine properties of Er-doped SnO_2 nanoparticles synthesized by a polymer precursor method are reported in this study. X-ray diffraction patterns of samples doped with erbium up to 10 mol % indicate the formation of the tetragonal rutile phase. The mean crystallite size shows a rapid decrease from ~12 nm for the undoped sample down to ~4 nm for the 10 mol % Er-doped sample. Structural changes as a function of the Er content, i.e., changes in the lattice constants, Sn–O bond distances and bond angles, strongly suggest the substitutional solution of Er^{3+} ions and the onset of oxygen vacancies throughout the SnO_2 lattice. No dipolar-magnetic interaction is determined from the Mössbauer spectra which are well resolved by fitting with a distribution of electric-quadrupole doublets. Changes observed in the quadrupole splitting as a function of the Er content have been associated to the local strain induced by the cationic size mismatch and oxygen vacancies. This local strain affects the lattice contribution of the electric field gradient. The linear increase of the isomer shift is assigned to the enhancement of the oxygen vacancies as the Er content is increased. It is found that the oxygen vacancies provide with conduction electrons to the Er-doped SnO_2 nanoparticulated system, therefore modifying its electronic properties.

Keywords Nanoparticles · Rare-earth doped semiconducting tin oxide · XRD diffraction · TEM images · Mössbauer spectroscopy

F. H. Aragón · J. A. H. Coaquira (✉) ·
S. W. da Silva · P. C. Morais
Núcleo de Física Aplicada, Institute of Physics, University of Brasília, Brasilia, DF 70910-900, Brazil
e-mail: coaquira.ja@gmail.com

P. Hidalgo
Faculdade Gama-FGA, Sector Central Gama, Universidade de Brasília, Brasilia, DF 72405-610, Brazil

R. Cohen · L. C. C. M. Nagamine
Instituto de Física, Universidade de São Paulo, Sao Paulo, SP 05508-090, Brazil

P. C. Morais
Department of Control Science and Engineering, Huazhong University of Science and Technology, Wuhan 430074, China

H. F. Brito
Instituto de Química, Universidade de São Paulo, Sao Paulo, SP 05508-000, Brazil

Introduction

Rare-earth doped SnO_2 semiconducting material has been of great scientific and technological interest while focusing on the development of new optoelectronic devices such as lasers, LEDs, and optical amplifiers (Sambasivam et al. 2010). Er^{3+} ions exhibit luminescence because of 4f core transitions which are

practically independent of the host matrix (Sambasivam et al. 2010; Kong et al. 2009). This luminescence have been associated to transitions between the first Er^{3+} ions excited state ($^4I_{13/2}$) and its ground state ($^4I_{15/2}$) yielding several emission lines laying within the visible and infrared ranges (Kong et al. 2009). Particularly, the intraionic emission of Er^{3+} ions centered at 1.54 μm coincides with the minimum loss region of silica-based optical fibers (Kong et al. 2009; Ravaro et al. 2007). It is known that the luminescence of rare-earth ions incorporated in a wide bandgap semiconducting matrix could be efficiently enhanced by exciton recombination. Besides, the thermal quenching of the rare-earth emissions at room temperature can be greatly reduced by dispersing rare-earth dopants in a wide bandgap semiconductor host such as SnO_2 (Sambasivam et al. 2010).

On the other hand, reports suggest that the equilibrium solubility limit of rare-earth ions in bulk SnO_2 is estimated to be $\sim$0.05 at% (Matsuoka et al. 1983). However, the synthesis of doped SnO_2 thin films or nanoparticles using several techniques has been obtained. It is known that the particles size reduction can modify the optical properties of the doped nanostructures and their solubility limit can be increased (Sambasivam et al. 2010; Kong et al. 2009). According to Sambasivam et al. (2010), a solid solution of Er atoms up to $x = 0.1$ can be obtained in $Sn_{1-x}Er_xO_2$ compounds. Furthermore, to the best of our knowledge, there are no studies about the dependence of the lattice constants as a function of the dopant content and the role played by the aliovalent dopants such as Er^{3+} substituting Sn^{4+} ions in the SnO_2 system. It is known that two scenarios are possible when doped SnO_2 nanoparticles are synthetized.

Solid solution regime

This regime can be expected when the doping process is carried out by an isostructural compound such as TiO_2 to form the $Sn_xTi_{1-x}O_2$ compound. In this scenario, both compounds show similar crystalline structure (rutile-like) and their lattice constants and unit cell volume vary as the dopant concentration is increased (Sensato et al. 2003), in agreement with the Vegard's law. In this case, the cations coordination number (CN = 6) preservation must favor the linear dependence of the lattice constant on the dopant concentration.

Surface segregation

Above the solid solution limit, the excess of dopant is predominantly located in a surface layer region. This surface segregation has been observed in transition-metal doped SnO_2 nanoparticles, with doping levels greater than $\sim$2–3 mol% (Hidalgo et al. 2005; Castro et al. 2005). Events such as the reduction of the surface energy as the dopant content is increased or structural mismatches because of ionic size differences or chemisorption processes related to the dopant nature (Kung 1991) can favor surface segregation. When this surface excess happens, any discernible change or no clear trend of the unit cell volume is expected as the dopant concentration is increased.

In this study, we present the investigation of the structural properties of Er-doped SnO_2 nanoparticles synthetized by a polymer precursor method. Besides that, the hyperfine properties determined from Mössbauer spectroscopy measurements are analyzed and discussed in accordance with the structural modifications induced by the Er doping.

Structural details of the rutile structure

SnO_2 is formed in the rutile-type structure with a space group $P4_2/mnm$. The tetragonal unit cell contains six atoms (two tin and four oxygen atoms). The tin atoms are positioned at $\vec{r}_{Sn_1} = 0\hat{i} + \hat{j} + 0\hat{k}$ and $\vec{r}_{Sn_2} = {}^1\!/_2a\hat{i} + {}^1\!/_2a\hat{j} + {}^1\!/_2c\hat{k}$, where $\hat{i}$, $\hat{j}$, $\hat{k}$ are the unitary vectors. The tin atoms have a coordination number of 6, meaning that they are surrounded by a flattened octahedron of six oxygen atoms which are positioned at $\vec{r}_{O_1} = ua\hat{i} + ua\hat{j} + 0\hat{k}$, $\vec{r}_{O_2} = -ua\hat{i} - ua\hat{j} - 0\hat{k}$, $\vec{r}_{O_3} = ({}^1\!/_2 + u)a\hat{i} + ({}^1\!/_2 - u)a\hat{j} + {}^1\!/_2c\hat{k}$, $\vec{r}_{O_4} = -({}^1\!/_2 + u)a\hat{i} - ({}^1\!/_2 - u)a\hat{j} - {}^1\!/_2c\hat{k}$, $\vec{r}_{O_5} = ua\hat{i} + ua\hat{j} + c\hat{k}$ and $\vec{r}_{O_6} = -ua\hat{i} - ua\hat{j} - c\hat{k}$ (Robertson 1979), where u is a variable parameter of the rutile structure. Figure 1a shows the atoms' positions and the Sn–O distances in the unit cell. According to the geometrical features of the flattened octahedron there are two Sn–O bond distances (d_1, d_2) given by:

$$d_1 = |\vec{r}_{Sn_2} - \vec{r}_{O_1}| = \sqrt{(1/2a - ua)^2 + (1/2a - ua)^2 + (1/2c)^2} = a\sqrt{2(1/2 - u)^2 + (c/2a)^2} \quad (1)$$

and

$$d_2 = |\vec{r}_{Sn_2} - \vec{r}_{O_3}| = \sqrt{(1/2a - (1/2 + u)a)^2 + (1/2a - (1/2 + u)a)^2 + (1/2c - 1/2c)^2} = ua\sqrt{2} \quad (2)$$

The basal plane of the flattened octahedron formed by O_1–O_2–O_5–O_6 oxygens contains four equal bond distances, d_1. The two other oxygens (apical oxygens) are bonded to the central Sn atom with a bond distance, d_2. Other important parameter to be considered is the bonding angle O–Sn–O (α) which is formed by two oxygens located on the basal plane of the octahedron (O_1 and O_5) and the central Sn atom (Sn_2), as shown in Fig. 1a. This angle is obtained from $\cos\alpha = \frac{2a^2(1-2u)^2 - c^2}{2a^2(1-2u)^2 + c^2}$ and is related to the bonding angle θ by: $\theta = \pi - \alpha$. The bonding angle formed by the central Sn, one apical oxygen and one basal plane oxygen is π/2.

Experimental

Er-doped SnO_2 nanoparticles were synthesized by a polymer precursor method (Pechini's method). In this method, the doped tin dioxide powder is obtaining by using the $SnCl_2{\cdot}H_2O$ and $Er(NO_3)_3$ as precursors. Samples with Er content up to 10 mol% are considered in this study. Detailed description regarding the sample preparation is reported elsewhere (Hidalgo et al. 2005). The phase formation and average particle size have been determined by X-ray diffraction (XRD) technique using a commercial diffractometer with Cu-Kα radiation. XRD data have been corroborated by transmission and scanning electron microscopy (TEM and SEM) experiments. Analyses of the chemical composition of the samples have been carried out by energy-dispersive X-ray spectroscopy (EDS) measurements using the SEM microscope. Mössbauer spectroscopy measurements were carried out using a constant acceleration spectrometer with a $Ca^{119}SnO_3$ as the radiation source. A natural Sn foil was used as the absorber for the calibration and the calibration error was estimated to be less than ≈0.5 %. All spectra were obtained at room temperature and the isomer shifts (IS) have been calculated with respect to $CaSnO_3$. The analyses of the spectra have been carried out using a least-square fitting routine, assuming a Lorentzian lineshape and considering the hyperfine

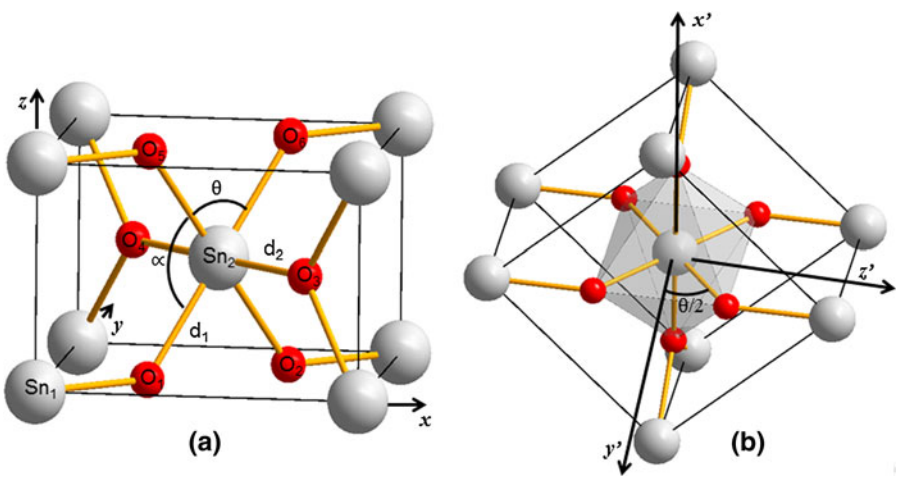

Fig. 1 **a** Schematic representation of the rutile crystalline structure of SnO_2. Oxygen atoms forming an octahedron around a Sn atom is shown. The O–Sn–O angles (∝ and θ) formed by the Sn–O bonds located in the basal plane of the octahedron are also shown. The main axes of the electric field gradient (EFG) are shown in part **b**

splitting of $I = 3/2, 1/2$ nuclear levels in the usual way (Gonser 1975).

Results and discussion

Structural and microscopic characterization

X-ray diffraction patterns of the Er-doped SnO_2 nanoparticles show reflections that are consistent with the cassiterite phase (rutile-type structure). The XRD data have been refined using the Rietveld refinement method. The analyses confirm the formation of the cassiterite phase and exclude the presence of other crystalline or amorphous phase. The lattice parameters of the undoped SnO_2 nanoparticles are $a = 4.7371$ Å and $c = 3.1867$ Å, which agree well with the standard data file (ICSD 39173; ICDD-PDF card No. 41-1445). The calculated and observed profiles of the XRD patterns of Er-doped SnO_2 nanoparticles are shown in Fig. 2. The linewidth (H) of the Bragg reflections shows an increasing tendency as the Er content is increased. This finding has been attributed to the crystallite size reduction and to the presence of residual strain (Aragón et al. 2010). To investigate these properties, the peak shape has been modeled using the Thompson–Cox–Hastings pseudo–Voigt function $\mathrm{TCH} - pV = \mu L - (1-\mu)G$, where L and G represent the Lorentzian and Gaussian peak functions, respectively, whereas μ is a mixing parameter (Aragón et al. 2010; Paiva-Santos et al. 2001). The line broadening related to the instrumental contribution was corrected by adequately subtracting the linewidth of a standard sample (Si single crystal) from the linewidth obtained from the refinement.

Assuming that the final linewidth (H) is related to both effects (the crystallite size and residual strain), the following relation can be used to evaluate both parameters:

$$H \cdot \cos\theta = K\lambda / <D> + 4\varepsilon \cdot \sin\theta \qquad (3)$$

here, $<D>$ is the mean crystalline size, ε is the residual strain and K is a dimensionless factor that depends on the particle shape ($K \sim 0.9$ for spherical shape). From the linear regression of $H{\cdot}\cos\theta$ versus $\sin\theta$ curve (Williamson–Hall plot), the mean crystallite size and the residual strain can be assessed.

Further corroboration of the XRD crystallite size has been obtained by TEM experiments. In Fig. 3a is shown a TEM image of the SnO_2 nanoparticles doped with 10 mol% Er. The histogram obtained after counting a large number of particles is presented in Fig. 3b. The histogram is well modeled by a log-normal distribution $f(D) = \left(\sigma D\sqrt{2\pi}\right)^{-1}\exp(-\ln[D/D_0]/2\sigma^2)$, represented by the solid line in the plot. Here, $\ln D_0$ is the average value of lnD (<lnD>) and σ is the size dispersion. Using $\sigma = 0.27$ determined from the fit, a $<D> = 5.8$ nm is obtained. This size is larger than the mean crystallite size determined from XRD data and suggests the occurrence of structural disorder located likely at the particle surface.

Figure 4 shows the plot of the mean crystallite size as a function of Er content. As observed in Fig. 4, the mean crystallite size shows a rapid decrease from ~12 nm, for the undoped sample, down to ~4 nm, for the 10 mol% Er-doped sample. This is an important effect of the doping, already observed in a number

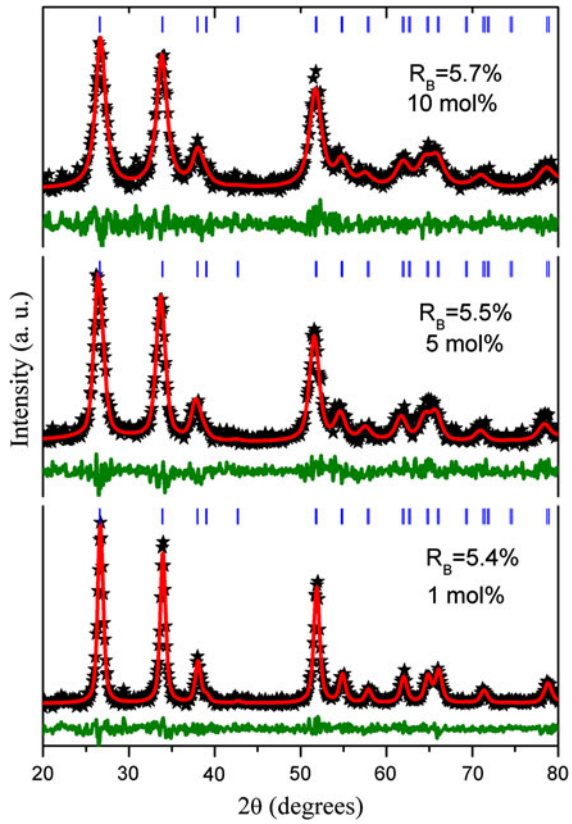

Fig. 2 X-ray diffraction (XRD) patterns of Er-doped SnO_2 nanoparticles. The observed and calculated data are represented by *stars* and *solid lines*, respectively. Differences between observed and calculated data are also shown. The quality of the refinements is represented by the R-factors

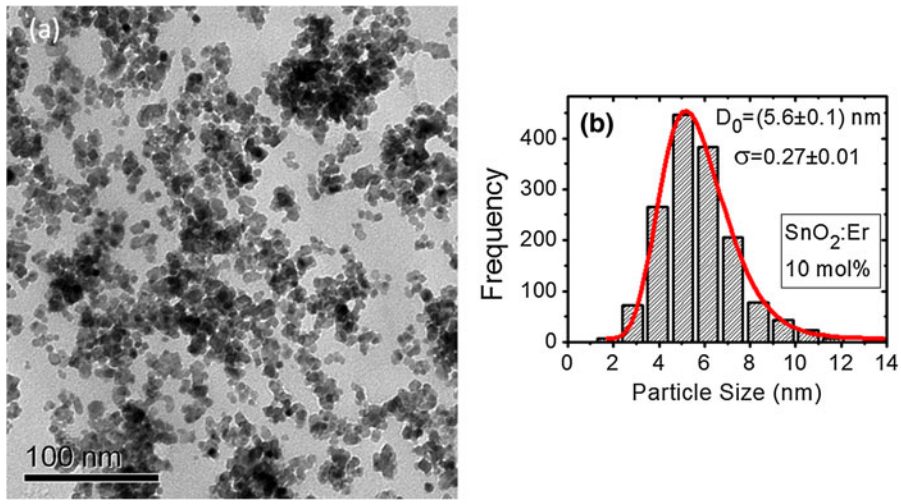

Fig. 3 **a** A TEM image of the SnO_2 nanoparticles doped with 10 mol% Er. In **b** the *vertical bars* represent the histogram of the particle size distribution and the *solid line* represents the log-normal function

of SnO_2 nanoparticulated systems doped with Ni, Fe and Mg (Hidalgo et al. 2005; Castro et al. 2005; Pereira et al. 2002). The particle size reduction has been associated with the surface segregation (surface excess) of dopant ions at the particle surface. Reports indicate that this segregation can be stabilized by the progressive decrease of the surface energy and can provide a barrier for the crystal growth diffusion mechanism (Hidalgo et al. 2005; Pereira et al. 2002).

The particle size reduction is accompanied by a decrease of the residual strain (see Table 1). The systematic reduction shows by the residual strain is different from that found in Ni-doped SnO_2 nanoparticles synthetized via the same method (Aragón et al. 2010). In the latter case, the residual strain does not show any clear trend as the dopant content is increased. It seems plausible to expect larger residual strain for larger surface segregation, because it can lead to larger mismatch among the lattice constants of the particle's core and shell regions. However, the surface segregation of the dopant ions seems to be small in the Er-doped SnO_2 nanoparticles than that determined in Fe- or Ni-doped SnO_2 nanoparticles systems (Hidalgo et al. 2005; Castro et al. 2005). Strong evidences in favor of a solid solution regime are obtained for Er-doped SnO_2 nanoparticles as discussed in the following. Therefore, in this case, the residual strain must be related to both the generation of oxygen vacancies and site disorder throughout the crystal lattice.

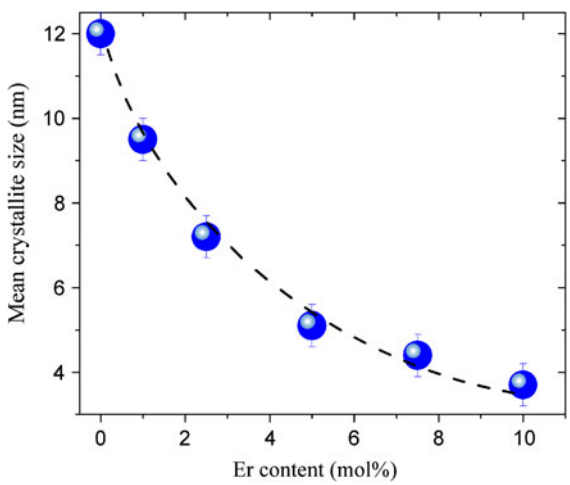

Fig. 4 Plot of the mean crystallite size as a function of the Er content in Er-doped SnO_2 nanoparticles. The *solid spheres* represent the experimental data and the *dashed line* is drawn to guide the eyes

A list of structural parameters obtained from the Rietveld refinements is presented in Table 1. The unit cell volume becomes larger as the Er content is increased. The same tendency is observed for both lattice constants. Whereas the *c*/*a* ratio also shows an increasing tendency as the Er content increases, the internal parameter of the rutile structure (u) tends to decrease. These opposite behaviors provide interesting structural changes into the intrinsically flattened octahedron of oxygen atoms surrounding the Sn atoms. The almost linear increase of the *c*/*a* ratio with the Er content indicates an anisotropic expansion of the unit cell along the *c* axis favored by the Er doping. A careful analysis of the octahedron symmetry indicates that the Sn–O distances in the basal plane

Table 1 List of parameters obtained from the Rietveld refinement of XRD data of Er-doped SnO_2 nanoparticles

Er content (mol%)	Er content (EDS, mol%)	Mean crystallite size (nm)	Residual strain (%)	*a* (Å)	*c* (Å)	*c*/*a*	*u* (Å)	Unit cell volume (Å^3)
0	–	12.0 ± 0.5	0.2050	4.7371	3.1867	0.6727	0.2968	71.510
1.0	0.9 ± 0.6	9.5 ± 2.0	0.3320	4.7391	3.1893	0.6729	0.3020	71.629
2.5	2.9 ± 0.9	7.2 ± 2.0	0.2227	4.7399	3.1908	0.6732	0.3001	71.687
5.0	5.9 ± 0.8	5.1 ± 2.0	0.1538	4.7430	3.1960	0.6738	0.2983	71.897
7.5	8.3 ± 0.6	4.4 ± 2.0	0.1448	4.7444	3.2014	0.6748	0.2953	72.061
10.0	10.1 ± 0.8	3.7 ± 2.0	0.1036	4.7467	3.2093	0.6761	0.2933	72.307

The Er contents determined from EDS measurements are also presented

(d_1) are slightly longer than the apical distances (d_2). The variations of these two distances are calculated using the refined parameters *a*, *c* and *u*. Figure 5 shows these variations as a function of the Er content. As the Er content is increased, the shorter Sn–O bond distance d_2 is shrinked and the longer bond distance d_1 is expanded. Besides, the angle θ (see Fig. 5a) shows a linear increase as the Er content is increased. These results indicate that the Er doping leads the octahedron to become more flattened while O–Sn–O angles of the basal plane (θ and α) tend to $\pi/2$.

Because no additional diffraction lines have been observed in the XRD patterns, the increase of the lattice constants strongly suggests that a solid solution has been attained. In this case, the substitution of Sn^{4+} ions by Er^{3+} ions leads to an increase in the lattice constants because of larger ions (r_{Er}^{3+}=0.881 Å) replacing smaller ions (r_{Sn}^{4+}=0.71 Å). This finding is in accordance with theoretical calculations (Freeman and Catlow 1990) that support the strong preference for the substitutional solution of trivalent, rare-earth dopants in SnO_2 and the creation of oxygen vacancies to achieve charge neutrality.

The variation of the lattice parameters can be modeled in the framework of the ion-packing model (Otobe and Nakamura 1999; Cosentino and Muccillo 2001). According to the structural properties of the rutile structure (see Fig. 1), the lattice constant *a* is given by:

$$a = \frac{1}{\sqrt{2}}(2r_c + 4r_a) \quad (4)$$

where r_c and r_a are the cationic and anionic radii, respectively. The solid solution of Er^{3+} ions into SnO_2 matrix, where only Sn^{4+} ions exist, is described by the formula $Sn_{1-x}Er_xO_{2-x/2}$, where *x* represents the Er content. This formula considers the generation of oxygen vacancies to keep charge neutrality. In this case, the ionic radii are given by:

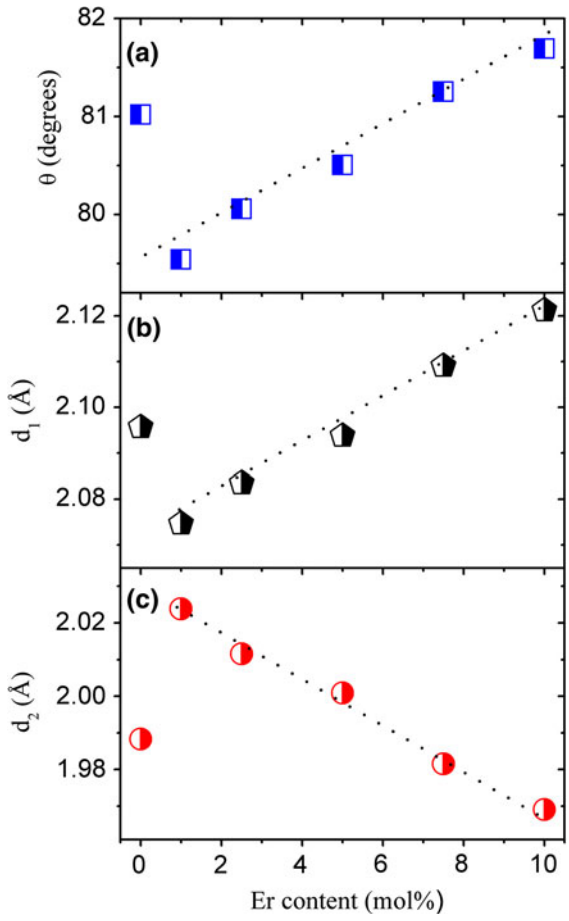

Fig. 5 Plot of the O–Sn–O angle (θ) and the interatomic distances (d_1 and d_2) as a function of the Er content in Er-doped SnO_2 nanoparticles

$$r_c = xr_{Er} + (1-x)r_{Sn} \quad (5)$$

$$r_a = (1-0.25x)r_O + 0.25xr_{Vo} \quad (6)$$

here, r_{Er}, r_{Sn}, r_O are the ionic radii of Er^{3+}, Sn^{4+} and O^{2-}, respectively and r_{Vo} is the radius of the oxygen vacancy. By substituting Eqs. 5 and 6 into Eq. 7 the following relation is determined:

$$a(x) = \sqrt{2}[(r_{Er} - r_{Sn} - 0.5r_O + 0.5r_{Vo})x + 2r_O + r_{Sn}] \quad (7)$$

For the undoped SnO_2 sample, Eq. 7 provides $a = 4.7376$ Å by substituting the ionic radii of O^{2-} (1.32 Å) and Sn^{4+} (0.71 Å). The validity of this model is assured because the calculated lattice constant is consistent not only with the value determined experimentally in this study ($a = 4.7371$ Å) but also with values reported in the literature: 4.737 Å (Baur and Khan 1971) and 4738 Å (Chang and Graham 1975).

The fit of the experimental values of a using Eq. 7 is shown in Fig. 6. As observed, a good linear regression is obtained when the radius of the oxygen vacancy is 1.11 Å. To our knowledge, no reported value of oxygen vacancy radius was found in the literature for the trivalent rare-earth doped SnO_2 system to compare with the value we obtained. However, the oxygen vacancy radius obtained in this study is comparable with that reported for trivalent rare-earth doped CeO_2 and ZrO_2 (Hong and Virkar 1995).

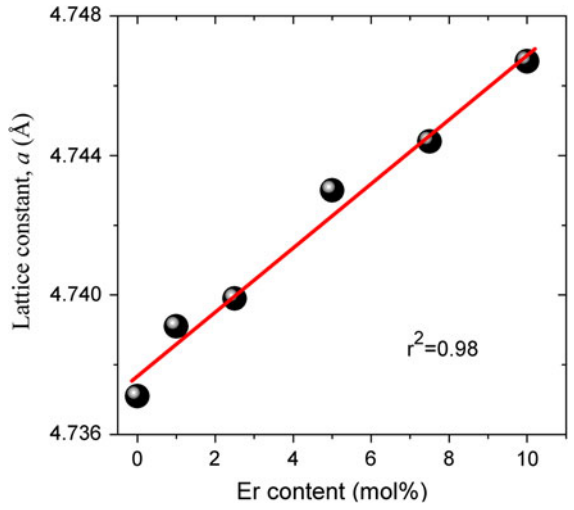

Fig. 6 Plot of the lattice constant a as a function of the Er content in Er-doped SnO_2 nanoparticles. Experimental data are represented by the *solid spheres*. The *solid line* represents the least-square fitting of data to Eq. 7. r represents the linear correlation coefficient

Mössbauer spectroscopy measurements

Room temperature Mössbauer spectra of the Er-doped SnO_2 nanoparticles are shown in Fig. 7. Careful analyses of these spectra indicate that no magnetic contributions (sextets) are present and, hence the spectra are well modeled by quadrupolar–electric interactions (doublets). Furthermore, fits using only one doublet provide a linewidth of $\Gamma \sim 2.0$ mm/s for the 1 mol% Er-doped SnO_2 nanoparticles. The observed linewidth slightly decreases as the Er content increases and becomes $\Gamma \sim 1.7$ mm/s for the 10 mol% Er-doped sample. The linewidths obtained from the fits are unusually larger when compared with values reported for bulk SnO_2 ($\Gamma \sim 0.9$ mm/s) (Stjerna et al. 1990). Those large values strongly suggest the presence of a distribution of quadrupole splitting (QS). Fits considering a histogramic distribution of QS are carried out and the results are shown in Fig. 7. The occurrence of the QS distribution could be associated to the several non-equivalent next nearest neighbor (nnn) coordination of Sn atoms. This scenario is enhanced by the occurrence of oxygen vacancies that produce strong local distortions. We choose the histogramic distribution (Brand 1990; Miglierini and Skorvánek 1991) to take into account all contributions.

The QS's distributions (see right-side panel of Fig. 7) show a slightly asymmetric shape and broad maximum centered in the low-QS region. The mean value of the QS distribution as a function of the Er content is plotted in Fig. 8. An average value, <QS> ~ 0.86 mm/s is found for the undoped sample. The <QS> shows a sudden increase, as soon as the Er ions are introduced into the SnO_2 matrix and reaches a value of ~ 1.02 mm/s for the 1 mol% Er-doped sample. Above that concentration, the <QS> show an almost linear decrease and becomes ~ 0.82 mm/s for the 10 mol% Er-doped sample. The <QS> versus Er content curve follows the same behavior observed in the residual strain versus Er content curve, as shown in Fig. 8. The increase of the <QS> observed in the low Er content region must be related to the local distortions arising because of the large mismatch between the ionic size of Er^{3+} and Sn^{4+} ions and the occurrence of oxygen vacancies, because of the difference in valence states.

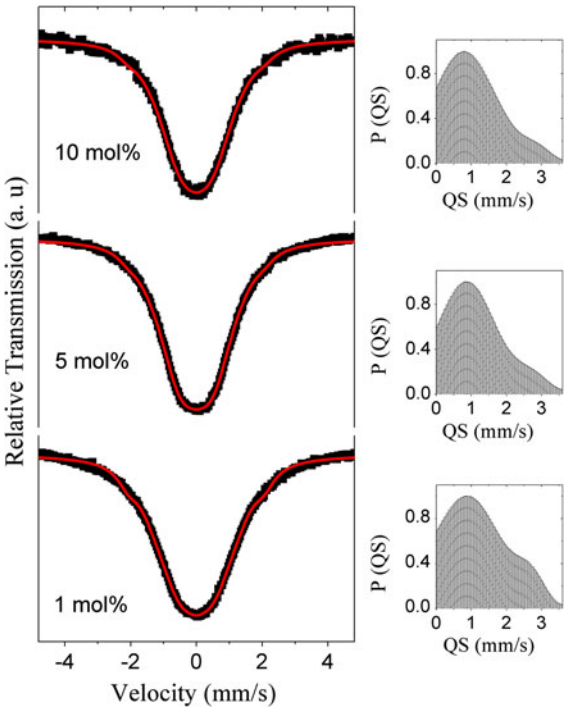

Fig. 7 Room-temperature Mössbauer spectra of Er-doped SnO_2 nanoparticles. *Points* represent the experimental data and *solid lines* represent the fit to a distribution of QS. The histogramic distributions of QS's are shown at the right-hand side panel

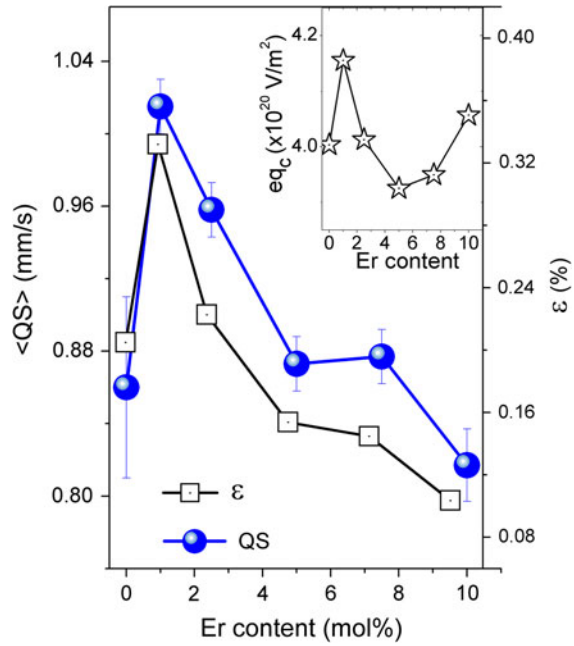

Fig. 8 The main panel shows the plot of the average quadrupole splitting (<QS>) and the residual strain (ε) as a function of the Er content. The inset shows the Er content dependence of $eq_c = eq_{latt} \times \left(1 + \frac{\eta^2}{3}\right)^{1/2}$, where eq_{latt}. represents the lattice contribution to the electric field gradient and η is the asymmetry parameter

The effect of the structural changes on the QS can be estimated by using the results obtained in the previous section. The QS is given by: $QS = \frac{e^2qQ}{2}\sqrt{1+\eta^2/3}$, where e is the elementary charge, eq is the electric field gradient, Q is the nuclear quadrupole moment of ^{119}Sn ($Q \sim 7$–13 fm^2 Barone et al. 2008; Huang et al. 1975) and η is the asymmetry parameter (Gonser 1975). For a crystalline solid, the eq has two contributions: the lattice charges and the aspherical distribution of valence electrons (Sen and Narasimhan 1977; Stöckler et al. 1966). An estimative of the lattice contribution (eq_{latt}) can be obtained using the point-charge model, the Sn–O distances (d_1 and d_2) and the angle θ of the octahedron around Sn atom (see Fig. 1). In the inset of Fig. 8, the calculated $eq_c = eq_{latt} \times \sqrt{1+\eta^2/3}$ is plotted as a function of the Er content. Although the calculated lattice contribution shows relatively smaller changes (up to ~ 5 %) than the changes of QS (up to ~ 20 %) as a function of the Er content, the maximum observed around 1 mol% is consistent with the larger QS value experimentally determined. Above ~ 5 mol%, the lattice contribution seems to become less important, likely because of the reduction of the local distortion. Furthermore, any additional change in the QS value must be related to the contribution of the eq_{val} term, which seems to be more important than the lattice term for higher Er content. The eq_{val} contribution cannot be simply calculated because the distribution of the valence electrons on the Sn atom in the Er-doped SnO_2 system is unknown. Therefore, first-principle calculations are required to determine the extent of the eq_{val} contribution.

On the other hand, the IS shows a linear increase as the Er content is increased >1 mol%, as shown in Fig. 9. The linear rate is estimated to be $dIS/dx \sim 0.25$ mm/s. This rate must be related to the particle size variation and to the Er content change. Therefore, the IS rate is given by:

$$dIS/dx = (\partial IS/\partial x)_D + (\partial IS/\partial D)_x (dD/dx) \quad (8)$$

here, $(\partial IS/\partial x)_D$ and $(\partial IS/\partial D)_x$ are the *IS* rate with respect to the particle size and Er doping changes, respectively. According to a previous study (Aragón

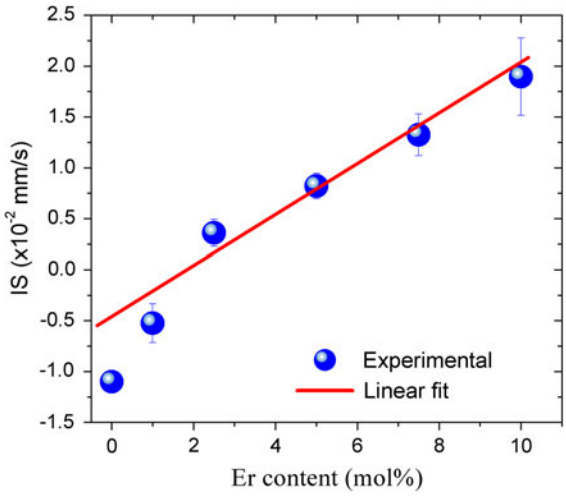

Fig. 9 Dependence of the isomer shift (IS) on the Er content. *Solid spheres* represent the experimental data and the *solid line* represents a linear fit

et al. 2011), although the size effect provides a negative rate of IS, an estimative of the particle size effect provides a negligible contribution. It means that the IS rate determined from the linear fit is related only to the doping effect and implies that the s-electronic density reaching the Sn nuclei throughout the crystal lattice increases as the Er content increases. The IS rate found for the Er-doping SnO_2 nanoparticles is almost twice the value found for Ni-doped SnO_2 nanoparticles (Aragón et al. 2011), where the solid solution of Ni ions is negligibly smaller and the surface segregation of Ni ions is the main event. The structural results obtained in this study strongly suggest the substitutional solution of Er ions and, consequently, the generation of oxygen vacancies in agreement with the results obtained in the previous section. The generation of oxygen vacancies favors the formation of SnO_2 compound as n-type semiconductor, i.e., more available conduction electrons are generated to the system (Stjerna et al. 1990). Therefore, the linear increase in the IS suggests a linear increase in the conduction electron density as the Er content is increased.

Conclusions

The structural characterization of Er-doped SnO_2 nanoparticles indicates the occurrence of substitutional solution of Er ions, i.e., the substitution of Sn^{4+} by Er^{3+} ions for samples with Er content up to 10 mol%. This low-valence substitutional solution favors the onset of oxygen vacancies to promote charge compensation. Although a negligible surface segregation of Er-dopants is expected in the Er-doped SnO_2 nanoparticulated system, its occurrence seems to be determinant to obtain smaller particles as the Er content is increased. The structural changes generated by the substitutional solution lead to important effects on the hyperfine properties. The Er content dependence of the average value of the QS has been related to the lattice contribution of the electric field gradient, which is found to be affected by the extent of the local strains. The linear increase of the IS as the Er content is increased has been assigned to the increase of the conduction electron density induced by the onset of oxygen vacancies.

Acknowledgments The authors thank the Brazilian agencies CAPES, CNPq, FAPESP and FAPDF for the financial support. The authors are grateful to Dr. E. M. Guimarães for carrying out X-ray diffraction measurements.

References

Aragón FH, Coaquira JAH, Hidalgo P, Brito SLM, Gouvêa D, Castro RHR (2010) Experimental study of the structural, microscopy and magnetic properties of Ni-doped SnO_2 nanoparticles. J Non Cryst Solids 356:2960–2964

Aragón FH, Cohen R, Coaquira JAH, Barros GV, Hidalgo P, Nagamine LCCM, Gouvêa D (2011) Effects of particle size on the structural and hyperfine properties of tin dioxide nanoparticles. Hyper Inter 202:73–79

Barone G, Mastalerz R, Reiher M, Lindh R (2008) Nuclear quadrupole moment of ^{119}Sn. J Phys Chem A 112:1666–1672

Baur WH, Khan AA (1971) Rutile-type compounds. IV. SiO_2, GeO_2 and a comparison with other rutile-type structures. Acta Cryst B 27:2133–2139

Brand RA (1990) User's guide of the Normos Mössbauer fitting program. Wissenschaftlich Elektronik GmbH, Duisburg

Castro RHR, Hidalgo P, Coaquira JAH, Bettini J, Zanchet D, Gouvêa D (2005) Surface segregation in SnO_2–Fe_2O_3 nanopowders and effects in Mössbauer spectroscopy. Eur J Inorg Chem 11:2134–2138

Chang ES, Graham EK (1975) The elastic constants of cassiterite as a function of pressure and temperature. J Geophys Res 80:2595–2599

Cosentino IC, Muccillo R (2001) Lattice parameters of thoria–yttria solid solutions. Mater Lett 48:253–257

Freeman CM, Catlow CRA (1990) A computer modeling study of defect and dopant states in SnO_2. J Solid State Chem 85:65–75

Gonser U (1975) Mössbauer spectroscopy. Springer, Berlin

Hidalgo P, Castro RHR, Coelho ACV, Gouvêa D (2005) Surface segregation and consequent SO_2 sensor response in SnO_2–NiO. Chem Mater 17:4149–4153

Hong SJ, Virkar AV (1995) Lattice parameters and densities of rare earth oxide doped ceria electrolytes. J Am Ceram Soc 78:433–439

Huang CH, Knop O, Othen DA, Woodhams FWD, Howie RA (1975) Pyrophosphates of tetravalent elements and a Mössbauer study of SnP_2O_7. Can J Chem 53:79–91

Kong J, Zhu H, Li R, Luo W, Chen X (2009) Carrier-mediated 1.55 μm photoluminescence from single Er^{3+} center in SnO_2 nanocrystals. Optics Lett 34:1873–1875

Kung HH (1991) Transition metal oxides: surface chemistry and catalysis, vol 45. Elsevier Science Publishing Company Inc., New York

Matsuoka T, Tohda T, Nitta T (1983) The low-energy-electron (LEE) excitation of SnO2: Eu powder phosphor; fundamental characteristics. J Electrochem Soc 130:417–423

Miglierini M, Skorvánek I (1991) Mössbauer and AC susceptibility study of structurally modified Fe–Ni–Cr–Mo–Si–B-type metallic glasses. J Phys Condens Matter 3:2721–2727

Otobe H, Nakamura A (1999) Lattice parameters and defect structure of the fluorite- and C-type oxide solid solutions between MO_2 and M_2O_3. Proceedings of the sixth international symposium on solid oxide fuel cells. The Electrochemical Society Inc., New Jersey

Paiva-Santos CO, Cavalheiro AA, Cilense MA, Varela JA, Silva MT, Mascarenhas YP (2001) An XRD study of the structure and microstructure of the laboratory synthesized crystals of $MgNb_2O_6$ (MN) and $PbMg_{1/3}Nb_{2/3}O_3$ (PMN). Adv X-Ray Anal 44:38–43

Pereira GJ, Castro RHR, Hidalgo P, Gouvêa D (2002) Surface segregation of additives on SnO_2 based powders and their relationship with macroscopic properties. Appl Surf Sci 195:277–283

Ravaro LP, Morais EA, Scalvi LVA, Li MS (2007) Visible emission from Er-doped SnO_2 thin films deposited by sol-gel. Cerâmica 53:187–191

Robertson J (1979) Electronic structure of SnO_2, GeO_2, PbO_2, TeO_2 and MgF_2. J Phys C 12:4767–4776

Sambasivam S, Kim SB, Jeong JH, Choi BC, Lim KT, Kim SS, Song TK (2010) Effect of Er^{3+} doping in SnO_2 semiconductor nanoparticles synthesized by solgel technique. Curr Appl Phys 10:1383–1386

Sen KD, Narasimhan PT (1977) Sternheimer antishielding factors for core electrons in metals: comparison with free-ion results. Phys Rev A 16:1786–1788

Sensato FR, Custodio R, Longo E, Beltrán A, Andrés J (2003) Electronic and structural properties of $Sn_xTi_{1-x}O_2$ solid solutions: a periodic DFT study. Catal Today 85:145–152

Stjerna B, Granqvist CG, Seidel A, Häggström L (1990) Characterization of rf-sputtered SnOx thin films by electron microscopy, Hall-effect measurement, and Mössbauer spectrometry. J Appl Phys 68:6241–6245

Stöckler HA, Sano H, Herber RH (1966) Mössbauer-effect studies of weak nuclear quadrupole interactions in 119Sn. J Chem Phys 45:1182–1189